ACS APPLIED ENERGY MATERIALS

www.acsaem.org Article

Ion-Assisted Ligand Exchange for Efficient and Stable Inverted $FAPbI_3$ Quantum Dot Solar Cells

Yuanze Xu, Hao Li, Shripathi Ramakrishnan, Donghoon Song, Yugang Zhang, Mircea Cotlet, and Qiuming Yu*

Cite This: https://doi.org/10.1021/acsaem.2c01565 Read Online

ABSTRACT: Perovskite quantum dot (QD) has emerged as a promising material for photovoltaics with its superior stability compared to their three-dimensional bulk counterparts, owing to its thermodynamically stabilized photoactive phase. However, ligand management on perovskite QD surfaces is extremely difficult due to the ionic nature of the perovskite lattice, which often leads to either incomplete removal of the native insulating ligands or formation of trap states during the ligand-exchange process, greatly hampering the photovoltaic performances. In this work, we report an ion-assisted ligand-exchange method for $FAPbI_3$ QDs using A-OAc (A = formamidinium (FA^+), guanidinium (GA^+), and phenethylammonium (PEA^+), OAc = acetate), with the A^+ and OAc^- ions promoting the removal of native long-chain insulating ligands. The more complete ligand exchange results in dense and well-oriented packing of QDs, together with the enhancement of electronic coupling and charge transport across QDs. In addition, the A^+ and OAc^- ions can fill the surface A-/X-site vacancies, respectively, reducing the QD surface trap state density and hence suppressing charge recombination and iodide migration. The p−i−n inverted QD solar cells fabricated with this ligand-exchange method exhibit significant enhancement in short-circuit current density (J_{SC}), reaching a PCE of 10.13%. Moreover, unencapsulated devices show impressive stabilities of more than 7300 h (10 months) storage time in a N_2-filled glovebox.

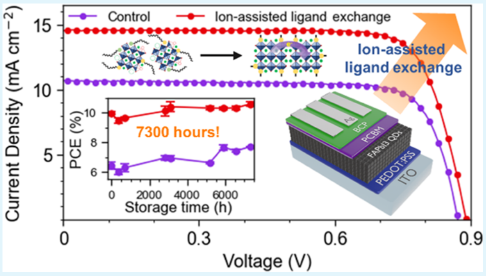

KEYWORDS: *perovskite, quantum dot, solar cell, ligand exchange, stability*

INTRODUCTION

Organic−inorganic halide perovskite (OIHP) has emerged as one of the most promising materials to replace silicon for photovoltaics, with the rapid progress in power conversion efficiency (PCE) from 3.9 to 25.8% over the past decade.[1] The high PCEs are attributed to the superior properties of OIHP, such as high absorption coefficients, low trap state densities, and long charge carrier diffusion lengths.[2−4] Among the choices of OIHP compositions, the prototypical methylammonium lead triiodide ($MAPbI_3$) has been extensively studied. However, due to its intrinsic moisture and thermal instabilities,[5,6] it is not an ideal option for high performance and stable solar cells. More recent record-breaking perovskite solar cells mostly contain α-phase formamidinium lead triiodide ($FAPbI_3$)-dominated compositions[7] because of their longer carrier lifetime, higher thermal stability, and more suitable band gap for single-junction solar cells.[8] Nonetheless, for $FAPbI_3$, the photoactive black α-phase can quickly transform into the photoinactive yellow δ-phase at room temperature, seeking for the lowest free energy of formation by strain relaxation.[9] Mixing A-cations such as MA^+, Cs^+, or Rb^+ has been proved to stabilize the photoactive perovskite phases,[10−12] but the long-term stability is limited due to light-induced ion segregation. When ions segregate, the locally pure perovskite phases will lose the stability offered by mixed composition and can then undergo phase transition, partially and over a long time completely degrading the film.[13]

Perovskite quantum dot (QD), as a nanostructured form of perovskites, offers a promising approach to solve the phase instability issue. As the crystal size decreases, the surface-area-to-volume ratio increases; thus, the increased surface energy significantly shifts the Gibbs energy profile, lowering the phase transition temperature and making photoactive phases stable at room temperature.[14,15] Recent works have demonstrated perovskite QD solar cells (QDSCs) based on phase-stable α-$CsPbI_3$ QDs and α-$FAPbI_3$ QDs.[16,17] Compared to their bulk counterparts, perovskite QDSCs usually possess a low open-circuit voltage (V_{OC}) deficit but large short-circuit current (J_{SC}) loss,[18] which highlights the importance of charge transport improvement and defect reduction in the research of perovskite QDSCs. Perovskite QD consists of a perovskite nanocrystalline core and an organic ligand shell, usually composed of both oleate (OA^-) and oleylammonium

Received: May 21, 2022
Accepted: July 26, 2022

(OAm^+). The ligands are used to control the growth of QDs during the hot-injection synthesis, offer colloidal stability, and passivate surface defects. However, these insulating long-chain ligands will greatly impair the charge transport and are therefore needed to be exchanged with conductive small ligands to construct efficient QDSCs.[19] Due to the ionic nature of the OIHP lattice, the ionic interaction between A^+ cation and the $[PbX_4]^{2-}$ sublattice is weak.[20] Traditional ligand-exchange methods developed for III−V and II−VI semiconductor QDs are too harsh and often cause the formation of defects or even decomposition of OIHP QDs. Methyl acetate (MeOAc) has been commonly used as an antisolvent for ligand exchange of OHIP QDs because of its optimum polarity that can remove the native oleate ligands while maintaining the OIHP QDs from decomposition.[16,21] So far, many works rely on MeOAc solutions of lead nitrate ($Pb(NO_3)_2$) for ligand exchange of OHIP QDs and have produced state-of-the-art high-performance perovskite QDSCs.[22] While $Pb(NO_3)_2$ has a potential to passivate the B-site defects, the underlying mechanism is still unresolved. The MeOAc solutions of amines have also been explored to facilitate the ligand exchange by acylation reaction.[23] Additionally, electron transport materials, such as $PC_{61}BM$[24] and ITIC,[25] have also been employed in the ligand-exchange step to enhance the charge transport.

In this work, we report an ion-assisted ligand-exchange method for $FAPbI_3$ QDs using MeOAc solutions of A-OAc, where A-cations are formamidinium (FA^+), guanidinium (GA^+), and phenethylammonium (PEA^+). We hypothesize that the A^+ cations and OAc^- anions can replace the native long-chain insulating OAm^+ and OA^- ligands and passivate the A^+ and X^- surface defects, respectively. As the A-site cation in the $FAPbI_3$ QD core, FA^+ can maintain a consistent lattice structure along the grain boundary, enabling the merging of exposed facets. GA^+ has a strong affinity to OIHP grain boundaries due to its higher tendency to form hydrogen bonding.[26] PEA^+ is a bulk cation that can effectively passivate OIHP surface defects and impose a dielectric confinement when anchored onto the grain boundaries.[27] We demonstrate that, as compared to pure MeOAc, QD films ligand-exchanged with the assistance of A-OAc show more complete removal of the native insulating OAm^+ and OA^- ligands, subsequently promoting dense and oriented packing of QDs. Taking these structural advantages, these QD films also exhibit enhanced charge transport across the QD films and reduced trap state density. The p−i−n $FAPbI_3$ QDSCs fabricated with A-OAc ligand-exchanged QD films show greatly enhanced J_{SC} and an improved PCE of 10.13%. Moreover, the QDSCs exhibit significantly enhanced device stability compared to their bulk counterparts. Unencapsulated devices remain stable after 7300 h (10 months) of storage in a N_2-filled glovebox. This work has opened a promising avenue to develop long-term stable perovskite solar cells.

■ EXPERIMENTAL METHODS

Chemicals. Oleylamine (OAm, 70%), oleic acid (OA, 90%), 1-octadecene (ODE, 90%), octane (anhydrous, 99%), hexane (95%), methyl acetate (MeOAc, anhydrous, 99.5%), ethyl acetate (EtOAc, anhydrous, 99.8%), formamidinium acetate (FAOAc, 99%), phenylethylamine (PEA, 99%), acetic acid (99%, aqueous solution), ethanol (99.5%), diethyl ether (99%), chlorobenzene (anhydrous, 99.8%), [6,6]-phenyl C61 butyric acid methyl ester (PCBM, 99.5%), and bathocuproine (BCP, 99.99%) were purchased from Sigma-Aldrich (St. Louis, Missouri) without further purification. Formamidinium iodide (FAI) was purchased from Greatcell Solar (Queanbeyan, Australia) without further purification. Lead(II) iodide (PbI_2, 99.99%) was purchased from TCI Chemicals. Poly(3,4-ethylenedioxythiophene):polystyrenesulfonate (PEDOT:PSS, CLEVIOS P VP AI 4083) was purchased from Heraeus.

Synthesis and Purification of $FAPbI_3$ QDs. In a 50 mL three-neck round-bottom flask, 1.04 g of FAOAc and 20 mL of OA were mixed and degassed under vacuum at 110 °C for 30 min. After a clear solution was obtained, N_2 was flowed into the flask. The FA−oleate solution was cooled to 80 °C and ready for injection. In another 100 mL three-neck round-bottom flask, 516 mg of PbI_2, 30 mL of ODE, 4.5 mL of OA, and 4.5 mL of OAm were mixed and degassed under vacuum at 120 °C for 30 min. After a clear solution was obtained, N_2 was flowed into the flask and the PbI_2 solution was cooled to 80 °C. Then, 7.5 mL of the FA−oleate solution was swiftly injected into the PbI_2 solutions. After 5 s, the reaction was quenched with an ice bath. The colloidal solution was split equally into two centrifuge tubes. Six milliliters of MeOAc was added into each tube and then centrifuged at 8000 rpm for 30 min. The precipitated QDs were dispersed in 10 mL of hexane. Ten milliliters of MeOAc was added into the QD hexane solution and then centrifuged at 8000 rpm for 10 min. The resulting precipitate was redispersed in 10 mL of hexane and stored in a refrigerator at 4 °C for at least 24 h before device fabrication.

Synthesis of PEAOAc. In a 250 mL round-bottom flask, phenylethylamine (10 mL, 80 mmol) was dissolved in 10 mL of ethanol in an ice bath. An acetic acid aqueous solution (9.73 mL, 170 mmol) was added dropwise to the flask with vigorous stirring. The mixture was kept in an ice bath for another 20 min until a colorless precipitate appeared. The precipitate was filtered and washed with diethyl ether. The crude precipitate was collected and recrystallized in ethanol twice to obtain thin, plate-like white crystals.

Deposition of QD Films. The QD solutions were centrifuged at 4000 rpm for 10 min. The supernatant was dried and redispersed into octane with a concentration of 60 mg mL^{-1}. A-OAc solutions were prepared by dissolving FAOAc, GAOAc, or PEAOAc into MeOAc. For each deposition of QD layers, the QD solution was spin-coated onto a substrate at 1000 rpm for 20 s and 2000 rpm for 5 s and then swiftly dipped into A-OAc solutions for 5 s. The QD films were then rinsed with neat MeOAc and dried under a stream of N_2. For solar cells, this process was repeated four times to stack ∼250 nm thick QD films. The films were then soaked in a saturated solution of FAI in EtOAc for 10 s, followed by rinsing with neat MeOAc and drying under a stream of N_2. All of the depositions were performed in ambient conditions with 30−40% relative humidity.

Device Fabrication. ITO-coated glasses (10 Ω sq^{-1} ITO, Colorado Concept Coatings LLC) with a size of 1.5 × 1.5 cm^2 were cleaned via sonication for 15 min in soapy DI water, DI water, acetone, and isopropanol in sequence, followed by 100 W plasma cleaning for 20 min. PEDOT:PSS solution was filtered through a 0.45 μm nylon filter. A drop of 70 μL of PEDOT:PSS solution was spin-coated onto a cleaned ITO glass at 4500 rpm for 40 s and then annealed at 145 °C for 20 min. The QD active layers were deposited following the procedure described above. The PCBM solution (20 mg mL^{-1} in chlorobenzene) was spin-coated onto the QD layers at 2000 rpm for 40 s without annealing. BCP solution (0.5 mg mL^{-1} in isopropanol) was spin-coated onto the PCBM layers at 4000 rpm for 40 s without annealing. Ag electrodes were deposited through thermal evaporation at 1×10^{-6} Torr at a rate of 2.0 Å s^{-1} for a total thickness of 100 nm.

Characterizations of QD Solutions and Films. Transmission electron microscope (TEM) images were acquired using an FEI Tecnai 12 BioTwin TEM. Ultraviolet−visible (UV−vis) absorption spectra were collected using an Agilent Cary 5000 UV−vis−NIR spectrometer. Steady-state photoluminescence (PL) and time-resolved photoluminescence (TRPL) were measured using an Edinburgh FLS1000 Spectrometer. Fourier transform infrared (FTIR) spectra were collected using a Bruker Vertex V80V Vacuum FTIR system. Grazing-incident wide-angle X-ray scattering (GIWAXS) measurements were conducted at the Complex Materials Scattering (CMS, 11-BM) beamline of the National Synchrotron

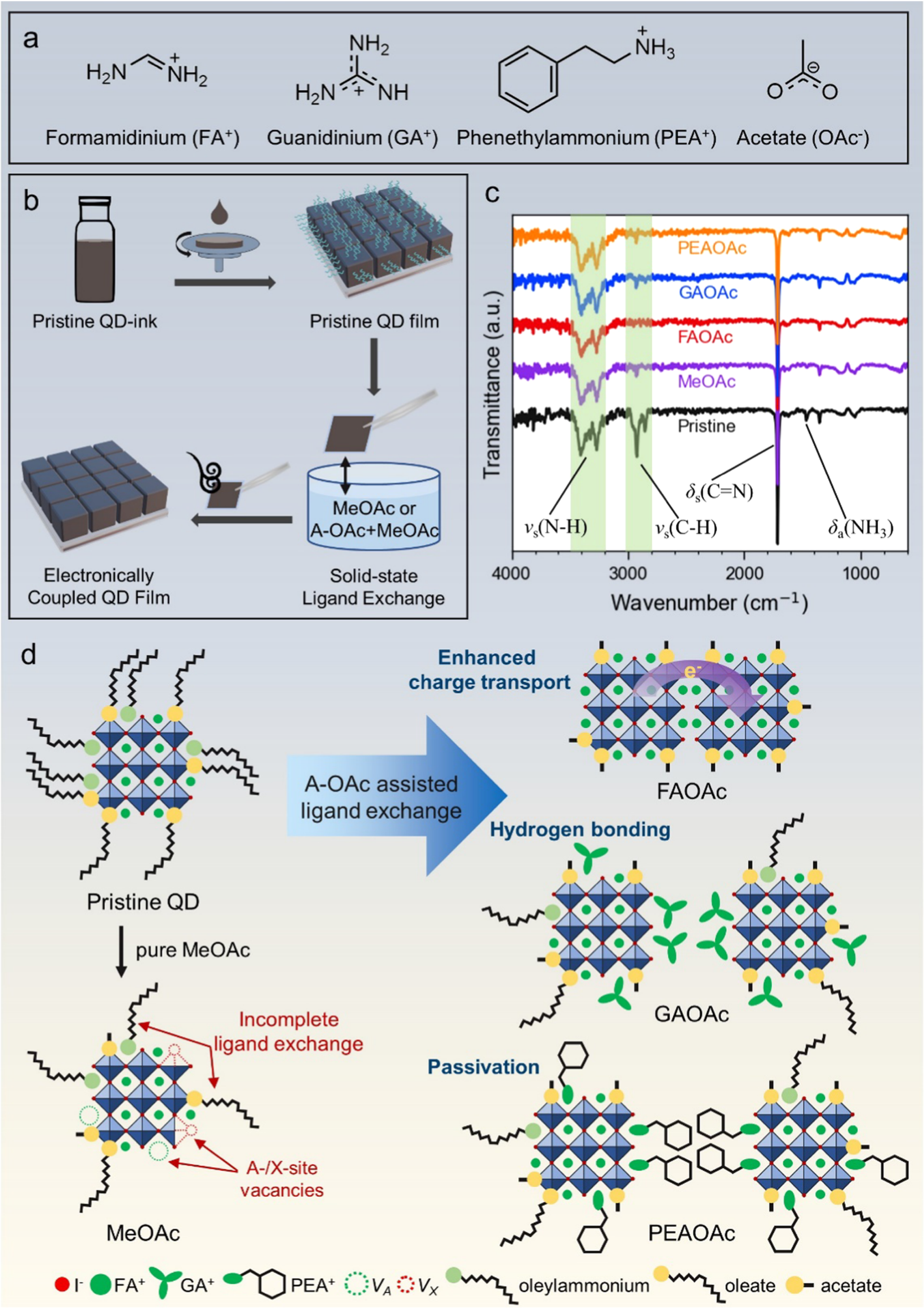

Figure 1. (a) Chemical structures of A^+ cations and OAc^- anion in A-OAc salts (A = FA^+, GA^+, or PEA^+). (b) Schematic illustrations of the fabrication process of electronically coupled QD films by ion-assisted ligand exchange. (c) Fourier transform infrared (FTIR) spectra of the $FAPbI_3$ QD films before and after ligand exchange under different conditions. (d) Schematic illustrations of the surface composition of pristine and ligand-exchanged $FAPbI_3$ QDs.

Light Source II (NSLS-II) at Brookhaven National Laboratory. The X-ray beam had a size of 200 μm (horizontally) × 50 μm (vertically), a divergence of 1 mrad, and an energy of 13.5 keV with a resolution of 0.7%. The scattered data were collected with a customized Pilatus 800K area detector (Dectris, Switzerland), which consists of 0.172 mm square pixels in a 1043 × 981 array, placed ~0.260 meters downstream from the sample position. Pump−probe transient absorption (TA) spectroscopy measurements were performed on a Helios Fire spectrometer (Ultrafast Systems LLC) using fs-pulsed Pharos (1 mJ)/Orpheus/Lyra light conversion system as the regenerative amplifier/optical parametric oscillator/frequency doubler system for generating the probe and the pump lights at a repetition rate of 1 kHz. Pump light (400 nm) generated in the Orpheus/Lyra system depolarized prior to the sample, while the white light was generated using a percentage of the fundamental beam (1030 nm) focused on a sapphire crystal. An optical delay placed in the probe beam path provided a dynamic range of up to 7 ns and an overall temporal resolution down to the pulse width of the laser (190 fs). The pump average power was measured by an Ophir PD 300 power meter diode, and the beam size was measured by an Ophir SP920S beam profiling camera.

Characterizations of QD Solar Cells. The photocurrent density−voltage (J−V) measurements were conducted in a N_2-filled glovebox with a SS-F5-3A solar simulator (EnliTech). The J−V curves for all devices were measured by masking the active area using a metal mask with an area of 0.0324 cm^2. Before the measurements, the light intensity was calibrated to 100 mW cm^2 using a standardized National Renewable Energy Laboratory calibrated silicon solar cell. The EQE spectra were measured with a QE-RX system (EnliTech). Scanning electron microscope (SEM) images were acquired using a Zeiss Gemini 500 scanning electron microscope operated at 3 kV. The impedance spectra were measured by a commercial instrument (Autolab PGSTAT302N), for which a bias voltage of 0.8 V and an AC amplitude voltage of 10 mV (frequency range: ∼100−1 MHz) were applied to devices. This measurement was carried out under dark conditions and in a Faraday cage.

■ RESULTS AND DISCUSSION

We synthesized $FAPbI_3$ QDs using a modified hot-injection method,[28] yielding cubic-shaped QDs with an average size of 15.4 ± 2.4 nm, obtained from the transmission electron microscope (TEM) image (Figure S1). The pristine $FAPbI_3$ QDs dispersed in hexane exhibit a static photoluminescence (PL) emission peak at 785 nm and an absorption onset at 1.56 eV (Figure S2), which is more suitable for single-junction solar cells than most commonly used $CsPbI_3$ QDs ($E_g \sim 1.80$ eV) according to the Shockley−Queisser limit.[29] To fabricate electronically coupled QD films, we conducted ion-assisted ligand exchange using MeOAc solutions of A-OAc. The chemical structures of the A^+ cations and the OAc^- anion are provided in Figure 1a. The pristine QD-ink is spin-coated onto a substrate to form the pristine QD film (Figure 1b). The pristine QD film is then dipped into the ligand-exchange solution, containing either pure MeOAc or MeOAc solutions of A-OAc (A = FA^+, GA^+, or PEA^+), for 5 s and blew dry with a stream of N_2. The resulting electronically coupled QD film is about 70 nm thick, consisting of 4−5 QD monolayers. For simplification, the QD films and devices fabricated with ligand exchange using pure MeOAc and MeOAc solutions of FAOAc, GAOAc, and PEAOAc are called MeOAc, FAOAc, GAOAc, and PEAOAc film/devices, respectively.

Figure 1c shows the Fourier transform infrared (FTIR) spectra of QD films before and after ligand exchange under different conditions. The FTIR spectrum of the pristine film clearly shows the resonances of the oleyl group (ν_s(C═C−H) = 3005 cm^{-1}, ν_s(C−H_x) = 2780−3000 cm^{-1}).[21] The intensities of these peaks greatly drop for the MeOAc, GAOAc, and PEAOAc films, suggesting that most long-chain ligands are removed but some are still present at the $FAPbI_3$ QD surfaces. These peaks completely disappear in the FAOAc film, indicating that FAOAc can further promote the removal of the long-chain ligands to below the detection limit of FTIR. The N−H stretch peaks (ν_s(N−H)) at 3200−3400 cm^{-1} and the C═N bending peak (δ_a(C═N)) at 1710 cm^{-1} remain unchanged after ligand exchange because they are dominated by FA^+ from the QD cores, indicating that the lattice structure of the QD cores is intact. We attribute the characteristic resonance at 1465 cm^{-1} to the NH_3^+ asymmetric bending (δ_a(NH_3)) from OAm^+, which also completely disappears after the ligand exchange using FAOAc. Note that PEA^+ also has an NH_3^+ group and GA^+ has three NH_2^+ groups. Therefore, by judging the intensity of this peak in the GAOAc and PEAOAc films, it is hard to determine whether the exchange of OAm^+ is incomplete or GA^+/PEA^+ substituted the surface sites of OAm^+. Nonetheless, the FTIR results reveal that both cationic and anionic long-chain ligands can be more effectively removed by FAOAc compared with MeOAc, GAOAc, or PEAOAc.

As depicted in Figure 1d, the pristine $FAPbI_3$ QD is coated with long-chain cationic oleylammonium (OAm^+) and anionic oleate (OA^-) ligands, passivating the surface A-site and X-site, respectively. After ligand exchange with MeOAc, the long-chain ligands can only be removed partially, with the remaining ligands impairing the charge transport across the resulting QD films. In addition, as A-/X-site vacancies could be left behind where the long-chain ligands are removed, there are no cations to fill the A-site vacancies and only inefficient filling of X-site vacancies by OAc^- from the hydrolysis of MeOAc.[21] These vacancies usually function as the recombination sites to hamper the charge collection and the ion migration pathways to cause perovskite degradation.[13,30] When FAOAc is added to assist the ligand exchange, the free FA^+ cations and OAc^- anions can both effectively replace the long-chain OAm^+ and OA^- ligands and fill the A-/X-site vacancies. Moreover, exposed QD facets capped with small FA^+ and OAc^- could merge with each other, creating efficient charge transport channels across QDs. In the GAOAc and PEAOAc films, although the removal of long-chain ligands may be incomplete, the A- and X-site vacancies could be filled by GA^+/PEA^+ and OAc^-, respectively. The passivation of QD surfaces with short A^+ and OAc^- ligands will suppress the charge recombination and the iodide migration, greatly improving the photovoltaic performance and stability.

To investigate the crystal structures and the QD packing of the QD films before and after ligand exchange under different conditions, we conducted grazing-incidence wide-angle X-ray scattering (GIWAXS) measurements with the incident angle α_i varied from 0.05 to 0.25° to probe the structural uniformity from the top surface to the bulk of the QD films. The QD films were deposited with onespin-coating step and undergo different ligand-exchange conditions, resulting in ∼70 nm thick QD films, consisting of 4−5 monolayers of QDs. As shown in Figure S3, for all QD films, the GIWAXS patterns only show vague patterns for α_i = 0.05 and 0.10°, whereas the patterns with α_i = 0.15° show clear Debye−Scherrer rings. When α_i is increased to 0.20 and 0.25°, a wide background signal appears between q_r = 1.4 and 2.5 Å^{-1}, which mainly comes from the PEDOT:PSS coated on the substrate before depositing the QD films. This indicates that the critical angle α_c for $FAPbI_3$ QD films is around 0.15°. Therefore, for α_i = 0.05 and 0.10°, the penetration depth is smaller than twice the size of the QDs,[31] suggesting a reasonable surface roughness of 1−2 QDs of the QD films. For $\alpha_i \geq 0.15°$, the penetration depth is long enough to cover the bulk of the QD films, and

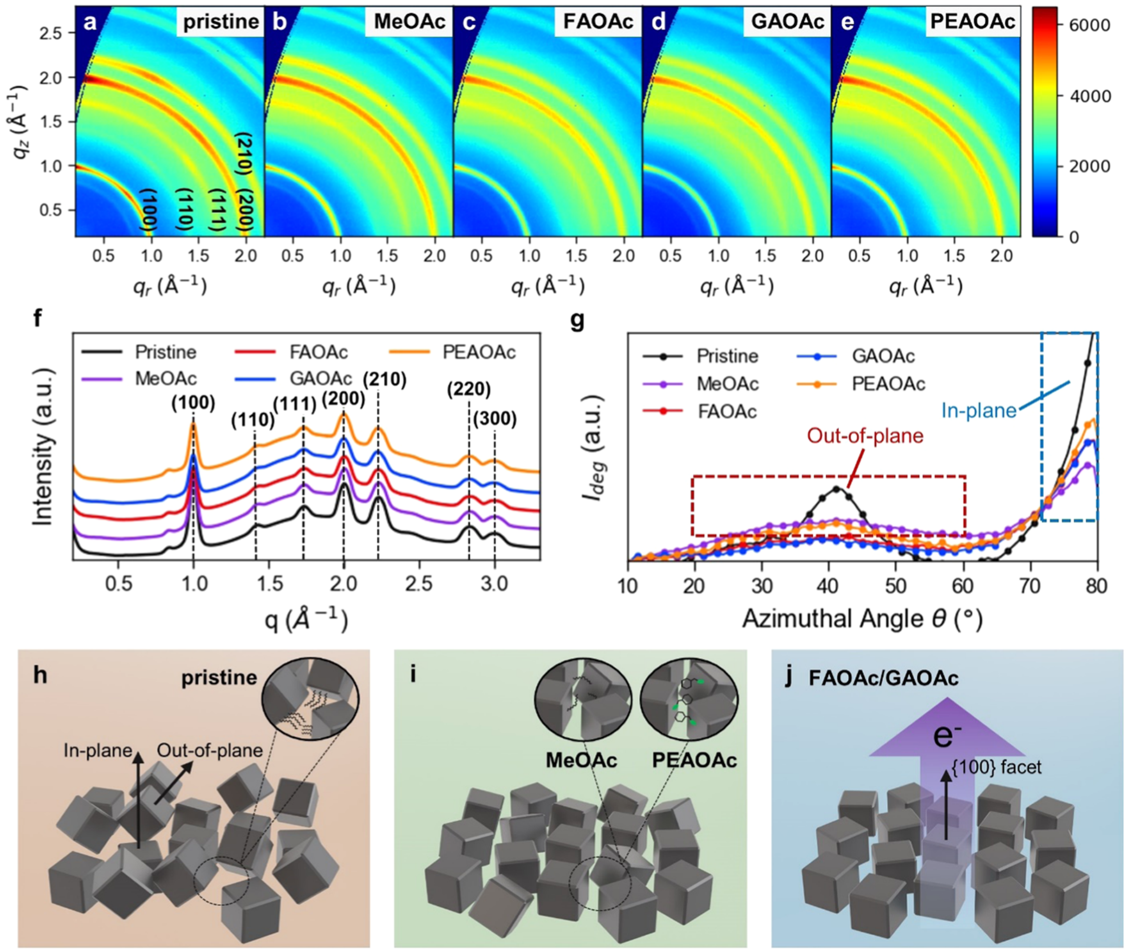

Figure 2. GIWAXS patterns of (a) pristine, (b) MeOAc, (c) FAOAc, (d) GAOAc, and (e) PEAOAc QD films. The incident angle α_i is 0.25°. (f) In-plane line-cut of the GIWAXS patterns. (g) Azimuthal angular averaged intensity for $q = 1$ Å^{-1}, corresponding to the (100) plane. Proposed packing and orientation modes of (h) pristine film, (i) MeOAc and PEAOAc films, and (j) FAOAc and GAOAc films. A single layer of QD, instead of 4−5 layers of QDs in the QD films, is illustrated for clearance.

the patterns show Debye−Scherrer rings located at identical q values, proving a structural uniformity across the QD films.

The GIWAXS patterns of the QD films with $\alpha_i = 0.25°$ are presented in Figure 2a−e. The q values of the Debye−Scherrer rings agree well with the bulk α-phase $FAPbI_3$ lattice.[32] The major peaks of the $FAPbI_3$ lattice are clearly resolved and labeled in the line-cut plot (Figure 2f), confirming that the α-phase of $FAPbI_3$ lattice is preserved and no additional perovskite phases are created after all ligand-exchange processes. The pristine film exhibits two spots in the ring associated with the (100) plane ($q = 1$ Å^{-1}) around azimuthal angles θ of 90 and 45° and another two spots in the ring associated with the (111) plane ($q = 1.7$ Å^{-1}) around θ = 90 and 45° as well, indicating two preferred orientations of the QD cores. The spots around 45° become weaker in the MeOAc and PEAOAc QD films and almost disappear in the FAOAc and GAOAc QD films, while the spots around 90° remain in all QD films. This indicates that the secondary preferred orientation around 45° is reduced or nearly eliminated after ligand exchange.

To further analyze the orientation change in the QD films, we conducted azimuthal conversion of the GIWAXS patterns (Figure S4). Since the cubic-shaped $FAPbI_3$ QDs usually have their {100} facets exposed,[33] the azimuthal angular averaged intensity of the (100) plane ($q = 1$ Å^{-1}) can serve as an indication of the orientations of individual QDs (Figure 2g). The pristine QD film shows two peaks at θ = 90 and 42°, revealing that QDs assemble in mainly two orientations, with their {100} facets facing perpendicularly upward (in-plane) or with a tilted angle (out-of-plane) to the substrate. This is attributed to the presence of long-chain ligands that separate adjacent QDs from the effective facet-to-facet interactions (Figure 2h). After the ligand exchange, the partial or complete removal of native long-chain ligands creates a void space between QDs, leading to a collapse of QDs toward the substrate. During this process, the out-of-plane QDs have a chance to adjust their orientations in the presence of strong interactions between exposed facets. In the MeOAc and PEAOAc films, the peak at θ = 42° is reduced to a weak and wide peak between θ = 20 and 60°. This suggests that the incomplete ligand exchange with pure MeOAc leaves some native long-chain ligands on the QD surfaces, which interferes with the packing of QDs (Figure 2i). While ligand exchange with PEAOAc can remove more native long-chain ligands, the bulky PEA^+ anchored on the QD surfaces could still prevent the QDs from ordered packing. This peak is further reduced after the ligand exchange with FAOAc and GAOAc. With FAOAc and GAOAc assisted ligand exchange, even more native long-chain ligands are removed from the QD surfaces. More importantly, the small size of FA^+ and GA^+, together

https://doi.org/10.1021/acsaem.2c01565
ACS Appl. Energy Mater. XXXX, XXX, XXX−XXX

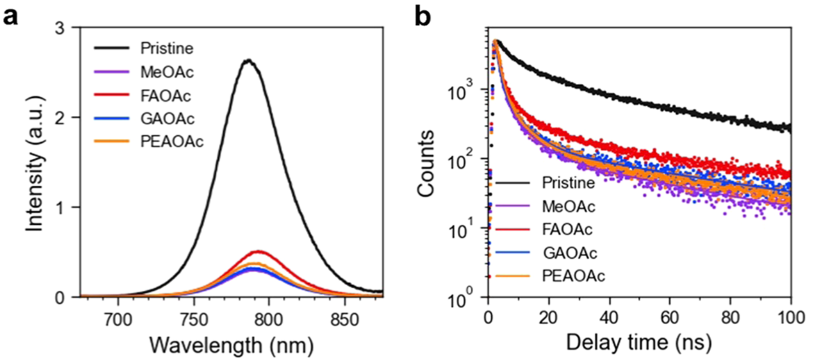

Figure 3. (a) Static PL emission spectra and (b) time-resolved PL spectra of the pristine, MeOAc, FAOAc, GAOAc, and PEAOAc QD films.

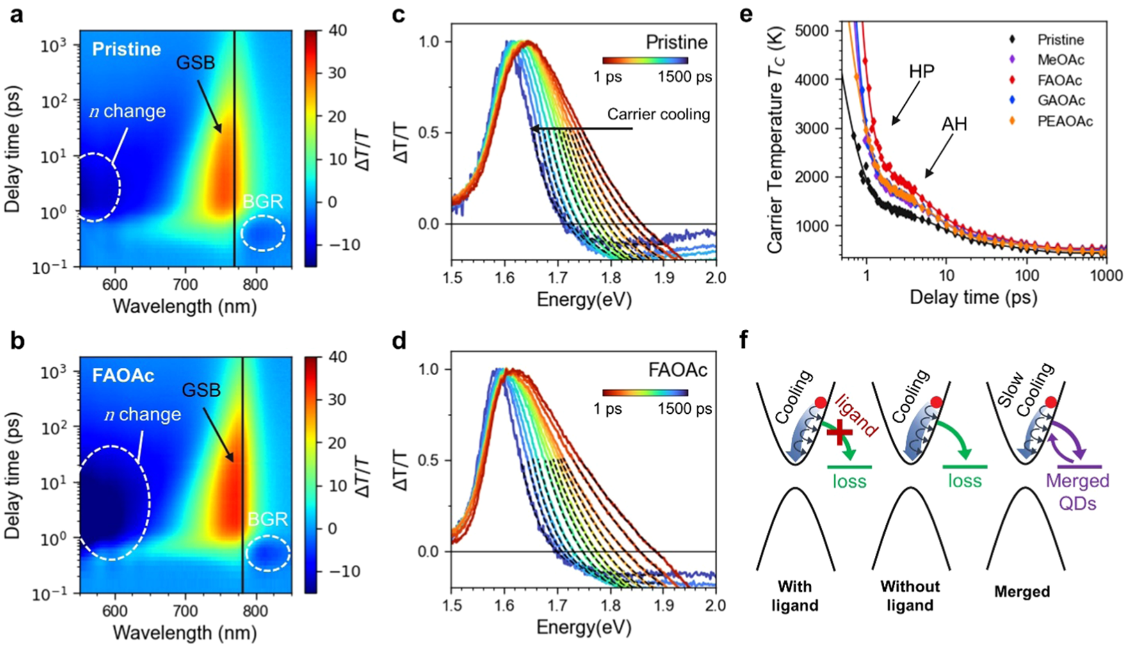

Figure 4. 2D heatmap transient absorption (TA) spectra of (a) pristine and (b) FAOAc films under 400 nm (3.10 eV) pump with a fluence of 11.9 μJ cm^{-2}, generating an initial carrier density of 2.39 × 10^{18} cm^{-3}. Normalized TA spectra ($\Delta T/T$) of (c) pristine and (d) FAOAc films at pump−probe delay times between 2 and 1500 ps. The black dashed lines are fits to the high-energy bleach tails with the Maxwell−Boltzmann distribution to extract the effective carrier temperature T_C. (e) Extracted carrier temperature T_C as a function of delay time for all QD films. (f) Schematic illustration of the hot carrier cooling mechanism and the hot phonon effect in the pristine and QD films with different ligand exchange.

with their stronger hydrogen-bonding capabilities, can promote the facet-to-facet interactions between QDs, resulting in more compact and orientated QD films (Figure 2j). When the QDs are aligned with a facet-to-facet matched orientation, a fast charge transport pathway across QDs will be created.[34] Moreover, the in-plane orientation will favor the charge transport and collection from the active layer to both electrodes along the vertical direction, significantly boosting the photovoltaic performance.[35]

We further investigate the photophysical properties of the QD films before and after ligand exchange under different conditions. The pristine film exhibits an absorption onset at 797 nm, which red-shifts to ∼800 nm after ligand exchange with MeOAc, GAOAc, and PEAOAc and to ∼802 nm with FAOAc, determined from the Tauc plots of the UV−vis spectra (Figure S5). The Gaussian distribution fitting plots of the normalized PL spectra reveal the same trend (Figure S6), where the PL peak red-shifts from 787 nm for the pristine film to ∼790 nm for the MeOAc, GAOAc, and PEAOAc films and 793 nm for the FAOAc film. As compared to the pristine film, the PL intensities of the ligand-exchanged films drop by over six times (Figure 3a), which agrees with previous reports on the PL quantum yield of QDs during each step of QDSC fabrication.[18] While the MeOAc and GAOAc films show similar PL intensities, the PEAOAc film shows slightly higher PL intensity, possibly due to the passivation effect of the surface-anchored PEA$^+$. The PL intensity of the FAOAc film is much higher than those of other ligand-exchanged QD films, indicating a better suppression of nonradiative recombination. This phenomenon rules out the possibility that the red shift of the PL peak is caused by the formation of sub-band-gap trap states, which should otherwise quench the PL intensity. Instead, when the long-chain ligands are replaced by FA$^+$ and OAc$^-$, exposed QD facets tend to merge due to the matched lattice at the QD grain boundary, slightly reducing the quantum confinement effect and hence causing a red shift of the band gap. In this case, excited electrons become delocalized and could further relax from the band edge of the QDs where they are generated to the minimum energy state available among the QDs in the delocalization range before going through radiative recombination. Therefore, the electronic coupling between QDs is enhanced, which will significantly improve the charge transport. We also carried out time-resolved PL (TRPL) measurements (Figure 3b). The TRPL curves are fitted with a triexponential model, and the averaged charge carrier lifetimes are calculated with an amplitude average method (Table S1).[36] The pristine film has a relatively long charge carrier lifetime of 19.88 ns due to the passivation effect of OAm^+ and OA^- ligands, which greatly drops when the long-chain ligands are removed after ligand exchange. The FAOAc film exhibits the longest charge carrier lifetime of 4.58 ns among the ligand-exchanged films, highlighting the superior passivation effect of FA^+. The PEAOAc and GAOAc films show the charge carrier lifetimes of 3.52 and 3.39 ns, respectively, higher than that of the MeOAc film (3.00 ns), which is attributed to the reduced trap-assisted nonradiative recombination by the A-site defect filling effect of PEA^+ and GA^+.

To further understand the enhanced electronic coupling between QDs and the defect passivation effect of ion-assisted ligand exchange, we conducted transient absorption (TA) measurements, under a 400 nm (3.10 eV) pump laser with a fluence of 11.9 μJ cm^{-2}, yielding an initial carrier density of 2.39×10^{18} cm^{-3} (see Supplementary Note 1 for calculations). The initial carrier density is known to have a direct impact on the hot charge carrier cooling dynamics.[37−39] The typical initial carrier density is in the range of $\sim 10^{17}$ to $\sim 10^{18}$–10^{19} cm^{-3} from low to high density. Since the absorption and the thickness of the QD films are similar, we assume the initial carrier density is similar for all QD films. The 2D TA heatmaps of the pristine film and the FAOAc films are presented in Figure 4a,b. Upon pump excitation, the pristine film exhibits a ground state bleaching peak (GSB, positive signal in $\Delta T/T$, where ΔT is the pump-induced change in probe transmission and T is the steady-state probe transmission) centered around the band gap at 770 nm (1.61 eV) due to the band-filling effect. The broad high-energy tails of the bleach peaks represent the hot carrier Fermi−Dirac distribution, and they gradually narrow as the carriers cool down when the delay time becomes longer. The red shift of the GSB peak along the delay time is assumed to be the tradeoff between the BGR effect (red shift) and the Burstein−Moss effect (blue shift).[40] Two negative signals in $\Delta T/T$ centered around 800 nm (1.55 eV) and shorter than 650 nm (>1.90 eV) represent photoinduced absorptions (PIAs), which arise from band gap renormalization (BGR, quickly vanishes within 1 ps) and the photoinduced refractive index change, respectively.[41] Compared to the pristine film, the FAOAc film exhibits a stronger and red-shifted GSB peak centered around the band gap at 780 nm (1.59 eV) and similar PIAs (Figure 4b). The 2D TA heatmaps of the MeOAc, GAOAc, and PEAOAc films display similar features observed in the pristine and FAOAc films (Figure S7). To closely compare all of the QD films, we plot the GSB peaks at 2, 100, and 1500 ps delay times (Figure S8) when the excited QD films go through the processes of hot electron cooling and recombination decay.[42] Within all of the time frames, the GSB peaks red-shift after ligand exchange with the most shift shown by the FAOAc film. Considering that under such a high carrier density (2.39×10^{18} cm^{-3}), any trap states are filled, the red shifts are unlikely to involve the creation and passivation of shallow trap states in the QD films. Instead, these red shifts further confirm that ion-assisted ligand exchange can promote the formation of charge transport channels between QDs by merging exposed facets, subsequently enhancing the charge delocalization within the QD films, particularly in the FAOAc QD film.

The surface defect and dielectric environment of perovskite QDs sensitively influence the cooling dynamics of hot carriers generated by the photons with energies higher than the band gap.[43,44] We conducted the study of hot carrier cooling dynamics in the QD films by extracting the effective carrier temperature T_C over the span of delay time. Upon pump excitation, the hot carriers first go through a thermalization process to establish a quasi-equilibrium that can be described by the Fermi−Dirac distribution. The thermalization process lasts more than 0.5 ps in the QD films (Figure S9), which is much longer than that in perovskite bulk films, mainly because of the high pump fluence and intrinsic slow thermalization process of perovskite QDs.[45] The distribution of carriers within an energy range sufficiently higher than the band gap can be approximated to the Maxwell−Boltzmann distribution[46]

$$\Delta T/T(E) \propto \exp(E_F - E/k_B T_C)$$

where E is the probe energy, E_F is the quasi-fermi level, k_B is the Boltzmann constant, and T_C is the effective carrier temperature. The T_C fittings with different regions of interest (ROIs) display similar results except in the range of 2−20 ps (Figure S9d), which originates from the improper approximation when the ROI gets closer to the band gap.[47] Figure 4c,d shows the Maxwell−Boltzmann fitting of the pristine and FAOAc films, respectively, with the ROI from where the normalized $\Delta T/T \leq 0.5$ to where $E \leq 1.9$ eV. The curves of the extracted T_C as a function of delay time for all QD films are presented in Figure 4e. The T_C curves can be well described by a triexponential fitting

$$T_C = T_0 + A_1 e^{-t/\tau_1} + A_2 e^{-t/\tau_2} + A_3 e^{-t/\tau_3}$$

All of the QD films display hot carrier lifetimes consistently in three regions, with τ_1 in the 0.15−0.3 ps range, τ_2 within 4−7 ps, and τ_3 > 50 ps (Table S2), corresponding to the scattering of LO phonons, hot phonon (HP) bottleneck, and Auger heating (AH).[46] The pristine and PEAOAc films exhibit larger τ_1, suggesting the effect of surface ligands, either native long-chain ligands or PEA^+, in preventing the damping of phonons.[48] This also leads to a stronger HP bottleneck effect, as revealed by their larger τ_2 (Table S2). Interestingly, the pristine film shows the longest τ_2 but remains lower T_C than the ligand-exchanged QD films, while the FAOAc film shows the shortest τ_2 and retains the highest T_C. In the FAOAc film, because the QDs are merged, their wave functions overlap to produce a denser distribution of electronic states, leading to a broader initial carrier distribution and higher T_C. In addition, the phonons can transfer across the merged facets, facilitating the reabsorption of phonon energy to slow down the cooling (Figure 4f). Despite the different behaviors in the HP region, all of the films show similar slopes in the AH stage. Since AH originates from the excitation of electron in the conduction band by the energy released from recombining another electron in the conduction band and a hole in the valence band, the dielectric environment has much less or no effect on AH.

Motivated by the effect of ion-assisted ligand exchange on promoting oriented QD packing, passivating surface trap states of QDs, and enhancing electronic coupling between QDs, we fabricated inverted $FAPbI_3$ QDSCs with a device architecture

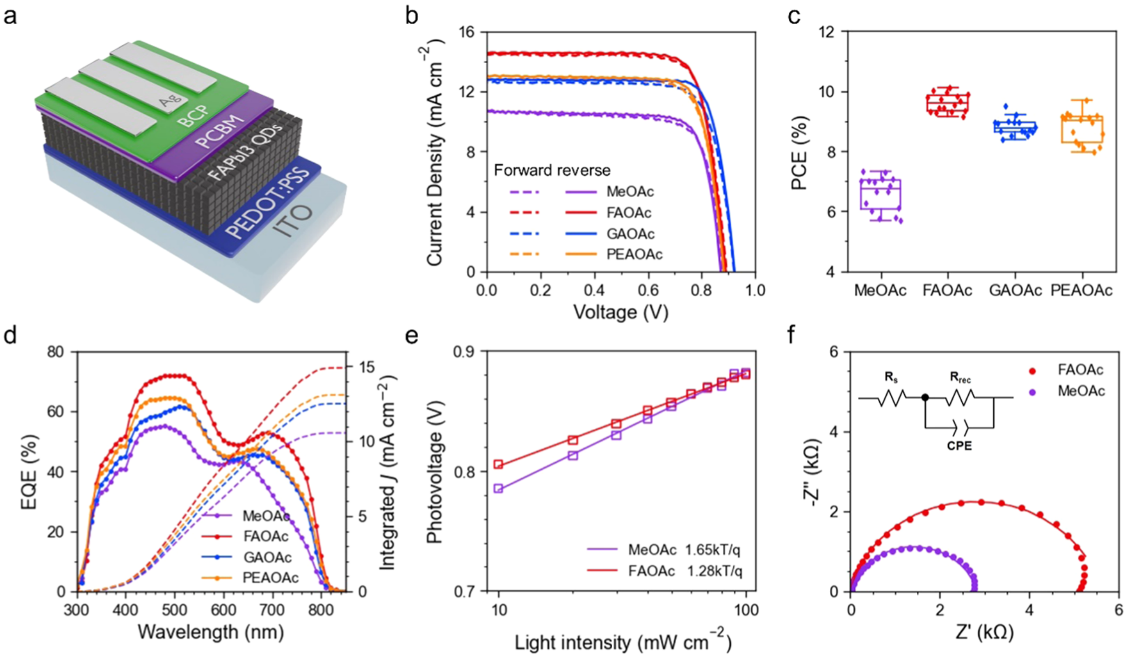

Figure 5. Device structure, performance, and physics of inverted $FAPbI_3$ QDSCs. (a) Schematic illustration of the inverted $FAPbI_3$ QDSCs. (b) The forward (dashed lines) and reverse (solid lines) scan $J-V$ curves of the best-performing QDSCs with different ligand-exchange conditions, measured under AM 1.5 G illumination at an intensity of 100 mW cm^{-2}. (c) PCE statistics of 16 devices for each ligand-exchange condition. (d) EQE spectra and the integrated photocurrent density plots of the best-performing QDSCs. (e) Light intensity-dependent V_{OC} for the FAOAc and the MeOAc devices. (f) The Nyquist plots of the FAOAc and the MeOAc devices measured under 0.8 V without illumination. The inset shows the equivalent circuit used to fit the Nyquist plots.

Table 1. Photovoltaic Parameters Obtained from the Reversed Scan $J-V$ Curves of Inverted $FAPbI_3$ QDSCs with Different Ligand-Exchange Conditions

sample		PCE (%)	J_{SC} (mA cm^{-2})	V_{OC} (V)	FF (%)
MeOAc	champion	7.29	10.65	0.87	78.5
	average	6.59 ± 0.55	10.27 ± 0.33	0.85 ± 0.01	75.0 ± 4.2
FAOAc	champion	10.13	14.56	0.89	78.6
	average	9.62 ± 0.29	14.33 ± 0.32	0.88 ± 0.02	76.7 ± 1.0
GAOAc	champion	9.52	12.79	0.92	81.1
	average	8.81 ± 0.27	12.29 ± 0.17	0.89 ± 0.01	81.3 ± 0.8
PEAOAc	champion	9.06	13.02	0.88	79.1
	average	8.79 ± 0.50	13.08 ± 0.46	0.87 ± 0.02	77.6 ± 2.9

of ITO/PEDOT:PSS/$FAPbI_3$ QD/PCBM/BCP/Ag (Figure 5a). The spin coating and ligand-exchange process were repeated fourtimes to stack ~250 nm thick QD films as the active layers, followed by a post-treatment of dipping into the saturated solution of FAI in ethyl acetate (EtOAc). To verify whether the remaining long-chain ligands by incomplete ligand exchange can cause QD films to partially redissolve when depositing the successive layers and lead to a thinner QD film, we measured the UV−vis spectra of QD films stacked after four deposition cycles for all ligand-exchanged QD films (Figure S10). The differences in light absorption of the QD films are negligible, indicating that all of the QD films have similar thicknesses. The top-view scanning electron microscope (SEM) images of the QD films are presented in Figure S11. For all of the conditions, dense QD films were obtained. The cross-sectional SEM image of one device is also shown in Figure S12. We varied the concentrations of FAOAc, GAOAc, and PEAOAc in MeOAc from 0.1 to 1.0 mM. The device photovoltaic parameters are summarized in Figure S13. The best-performing QDSCs are fabricated with 0.3 mM concentration for all three A-OAc salts. While high concentration solutions have less impacts on the performance of FAOAc and GAOAc devices, the PEAOAc devices display a significant decrease of V_{OC} and FF, possibly due to the formation of PEAI at the interface. Figure 5b shows the forward and reverse scan photocurrent density−voltage ($J-V$) curves of the best-performing MeOAc, FAOAc, GAOAc, and PEAOAc QDSCs. The photovoltaic parameters are summarized in Table 1. The MeOAc device exhibits a champion PCE of 7.29%, with a V_{OC} of 0.87 V, a J_{SC} of 10.65 mA cm^{-2}, and an FF of 78.5%. The J_{SC} and V_{OC} are increased to 14.56 mA cm^{-2} and 0.89 V, respectively, for the FAOAc champion device, leading to the highest PCE of 10.13%. Using GAOAc in MeOAc as the ligand-exchange solution yields a QDSC with a significantly boosted FF of 81.1%, an increased V_{OC} of 0.92 V but a lower J_{SC} of 12.79 mA cm^{-2}, resulting in a champion PCE of 9.52%. The PEAOAc device exhibits similar improvements in J_{SC} and V_{OC} to 13.02 mA cm^{-2} and 0.88 V, respectively, leading to a champion PCE of 9.06%. It is worth mentioning that all of the QDSCs exhibit negligible hysteresis, which reflects greatly suppressed iodide migration by X-site vacancy filling with OAc^-.[49] Additionally, the increases in V_{OC}

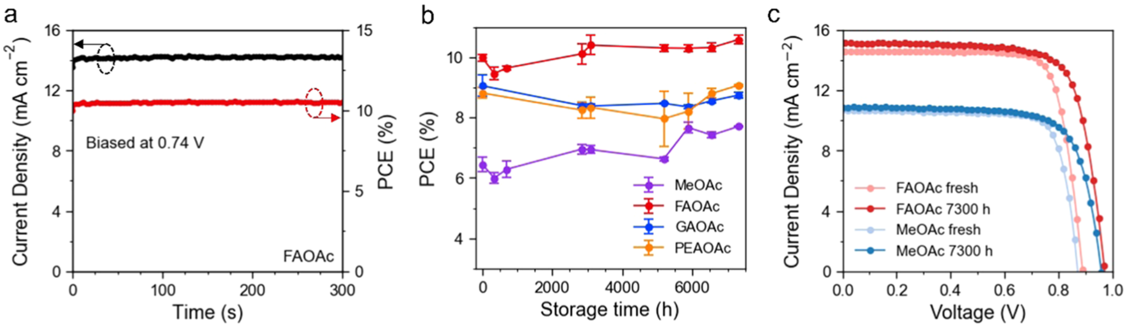

Figure 6. Short-term and long-term stabilities of inverted $FAPbI_3$ QDSCs. (a) The stabilized power output (SPO) and stabilized photocurrent density of the FAOAc device, measured at the maximum power point. (b) Long-term stability of the best-performing QDSCs that were stored in a N_2-filled glovebox without encapsulation. (c) Reverse scan $J-V$ curves of the MeOAc and FAOAc QDSCs that are freshly made and stored after 7300 h in a N_2-filled glovebox without encapsulation.

are attributed to the A-site passivation by the cations added in the MeOAc solutions. Compared to the published works on $FAPbI_3$ QDSCs (Table S3), which are n−i−p architecture devices, our champion p−i−n architecture device exhibits the highest FF and high J_{SC} but the V_{OC} is lacking behind other reported n−i−p $FAPbI_3$ QDSCs. It is possibly due to the unsatisfactory band alignment of the transport layers.

The statistics of PCEs and other photovoltaic parameters of 16 devices for each of the ligand-exchange conditions are presented in Figures 5c and S14, respectively. The average PCE is improved from 6.59% for the MeOAc devices to 9.75, 8.81, and 8.79% for the FAOAc, GAOAc, and PEAOAc QDSCs, respectively, confirming the improvement of device performance by ion-assisted ligand exchange. The statistics of photovoltaic parameters reveal that the performance improvement is mainly contributed by the increase of J_{SC} with a marginal increase in V_{OC} and FF. The FAOAc devices produce the highest average J_{SC}, indicating efficient charge transport across the QD film due to the efficient removal of long-chain ligands, passivation of surface vacancies, and electronic coupling of merged QD facets. The FAOAc and GAOAc devices exhibit high values and narrow distributions of FF, suggesting that the densely packed QD films can prevent the formation of shunt channels. We note that compared to the narrower distributions of J_{SC} and FF, V_{OC} exhibits relatively larger variance, which could be attributed to the in-ambient fabrication of QD films.

To better understand the photocurrent enhancement, the external quantum efficiency (EQE) spectra of the best-performing devices were measured (Figure 5d). All of the integrated photocurrent densities agree well with the J_{SC} measured from the $J-V$ curves. Compared with the MeOAc device, the GAOAc and PEAOAc devices display EQE increases in two spectral regions, 400−550 and 650−800 nm, and the FAOAc device exhibits a further increase in the full scope. The increases could be attributed to more efficient charge transport and longer carrier lifetime benefit from the effective removal of long-chain ligands and the passivation of trap states. We also note that the QD facets capped with FA^+ and OAc^- can merge to create fast charge transport pathways, which further enhances the EQE. In the 650−800 nm region, the FAOAc, GAOAc, and PEAOAc devices show steeper slopes than that of the MeOAc device, suggesting reduced recombination loss due to passivated trap states on QD surfaces. To further investigate the passivation of trap states by FAOAc ligand exchange, we conducted light intensity-dependent V_{OC} measurements on the FAOAc and the MeOAc devices (Figure 5e). The V_{OC} can be well described by $\ln(I)nkT/q$, where I, n, k, T, and q are the light intensity, the diode ideality factor, the Boltzmann constant, the device temperature, and the elementary charge, respectively. The diode ideality factors are calculated to be 1.28 and 1.64 for the FAOAc and the MeOAc devices, respectively. This indicates suppressed trap-assisted recombination in the FAOAc device compared to that in the MeOAc device, possibly due to the A-site vacancy filling effect of FA^+. The consistent results are attained from the measurement of impedance spectra. The Nyquist plots of the FAOAc and MeOAc devices are presented in Figure 5f, in which raw data points are fitted by an equivalent circuit model (shown in the inset). While only a single semicircle for recombination resistance (R_{rec}) appears for both,[50] the greater R_{rec} of 5600 Ω is resulted from the FAOAc device, nearly doubling the R_{rec} (2828 Ω) for the MeOAc device. This further proves the effective passivation effect of FAOAc on the QDSCs.

Figure 6a shows the short-term stability of the FAOAc device with a stabilized power output (SPO) of 10.5%, which is higher than the MeOAc device with a SPO of 7.5% (Figure S15). We also tested the long-term stability of unencapsulated QDSCs over a long storage time inside a N_2-filled glovebox. All of the QDSCs remained stable after 7300 h (Figures 6b and S16). Surprisingly, the FAOAc device performance is even increased after 7300 h storage (Figure 6c), with a significant increase in V_{OC} from 0.89 to 0.97 V, improving the PCE from 10.13 to 10.95%. The MeOAc device shows a similar increase in V_{OC} and PCE, but since the initial PCE is low, the PCE of the MeOAc device at 7300 h remains lower than the A-OAc ligand-exchanged QDSCs. The improved V_{OC} and high stability of the MeOAc device could be a result of the passivation effect by dipping the QD films into the solution of FAI in EtOAc and the remaining native long-chain ligands.[51] The superior device stability demonstrates the phase stability of α-phase $FAPbI_3$ at room temperature because of the lower phase transition temperature of $FAPbI_3$ QDs.[12,15] The effective removal of native long-chain ligands and passivation of surface A- and X-site defects by MeOAc solution of FAOAc further enhance the device performance while retaining high device stability.

There have been tremendous reports, and significant progresses have been made on perovskite QDSCs since its first demonstration in 2016.[52] While most of the works are based on $CsPbI_3$ QDSCs, with the best PCE of 16.5%,[53] the reports on $FAPbI_3$ QDSCs are limited.[52] As summarized in Table S3, all of the works on $FAPbI_3$ QDSCs are based on n−i−p device architecture, with the best PCE reaching 13.2%.[54] To the best of our knowledge, we are the first to report the p−i−n $FAPbI_3$ QDSCs and achieve a champion PCE of 10.13%. The p−i−n architecture features great long-term stability due to the exclusion of dopant in the transport layers. With more advanced synthetic methods of $FAPbI_3$ QDs and modifications of the interfaces, the performance of p−i−n $FAPbI_3$ QDSCs can be further improved while pertaining the superior device stability.

■ CONCLUSIONS

We report an ion-assisted ligand-exchange method with the MeOAc solutions of A-OAc (FAOAc, GAOAc, and PEAOAc) for $FAPbI_3$ QDs to simultaneously promote the removal of native long-chain ligands on QD surfaces and passivate the surface A-site and X-site vacancies. The MeOAc solutions of FAOAc yield the best ligand exchange of $FAPbI_3$ QDs in terms of the effective removal of native long-chain ligands, passivation of surface defects, and promotion of electronic coupling between QDs. Inverted $FAPbI_3$ QDSCs fabricated with this ligand-exchange method exhibit a significant J_{SC} enhancement, reaching a champion PCE of 10.13%. More importantly, all of the QDSCs exhibit superior device stabilities after storing in a N_2-filled glovebox without encapsulation for 7300 h (10 months). The FAOAc device even shows an increase in PCE from 10.13 to 10.95% after 7300 h. This work sheds light on the role of ionic salts in improving the packing and electronic coupling of $FAPbI_3$ QDs to boost the photovoltaic performance and provides a promising way to develop and construct ultrastable perovskite solar cells.

■ ASSOCIATED CONTENT

Supporting Information

The Supporting Information is available free of charge at https://pubs.acs.org/doi/10.1021/acsaem.2c01565.

> TEM image and size distribution of the QDs; Tauc plot and PL Gaussian fit of the colloidal QDs; GIWAXS patterns under α_i from 0.05 to 0.25° of the QD films; azimuthal GIWAXS patterns with $\alpha_i = 0.25°$; Tauc plot of the QD films; PL Gaussian fit of the QD films; 2D heatmap TA spectra of the MeOAc, GAOAc, and PEAOAc films; normalized TA spectra at a delay time of 2, 100, and 1500 ps; the TA spectra of the FAOAc film with a delay time from 0 to 2 ps; the Maxwell−Boltzmann fitting of the FAOAc film with different regions of interest; unnormalized UV−vis spectra of the QD films; top-view SEM images of the QD films; cross-sectional SEM image of one QDSC; photovoltaic parameters of QDSCs fabricated with different concentrations of A-OAc in MeOAc; statistics of the photovoltaic parameters for 16 $FAPbI_3$ QDSCs for each ligand-exchange conditions; stabilized power output of the MeOAc device; the evolution of photovoltaic parameters of the QDSCs over 10 months; triexponential fitting parameters of the TRPL; triexponential fitting parameters of the T_C decay; summary of the device architecture and photovoltaic performances of related works; and details of carrier density calculation (PDF)

■ AUTHOR INFORMATION

Corresponding Author

Qiuming Yu − *Robert Frederick Smith School of Chemical and Biomolecular Engineering, Cornell University, Ithaca, New York 14853, United States;* orcid.org/0000-0002-2401-4664; Email: qy10@cornell.edu

Authors

Yuanze Xu − *Robert Frederick Smith School of Chemical and Biomolecular Engineering, Cornell University, Ithaca, New York 14853, United States;* orcid.org/0000-0002-4873-6629

Hao Li − *Robert Frederick Smith School of Chemical and Biomolecular Engineering, Cornell University, Ithaca, New York 14853, United States;* orcid.org/0000-0002-9433-1198

Shripathi Ramakrishnan − *Robert Frederick Smith School of Chemical and Biomolecular Engineering, Cornell University, Ithaca, New York 14853, United States*

Donghoon Song − *Robert Frederick Smith School of Chemical and Biomolecular Engineering, Cornell University, Ithaca, New York 14853, United States;* orcid.org/0000-0003-0914-1507

Yugang Zhang − *Center for Functional Nanomaterials, Brookhaven National Laboratory, Upton, New York 11973, United States*

Mircea Cotlet − *Center for Functional Nanomaterials, Brookhaven National Laboratory, Upton, New York 11973, United States*

Complete contact information is available at: https://pubs.acs.org/10.1021/acsaem.2c01565

Author Contributions

The manuscript was written through contributions of all authors. All authors have given approval to the final version of the manuscript.

Notes

The authors declare no competing financial interest.

■ ACKNOWLEDGMENTS

This work was financially supported by NSF ECCS-2054942 and EPM-2114350. This work made use of the Cornell Center for Materials Research Shared Facilities, which are supported through the NSF MRSEC program (DMR-1719875). The GIWAXS and TAS experiments used the resources from the Centre for Functional Nanomaterials and the CMS beamline (11-BM) of the National Synchrotron Light Source II (NSLS-II), both supported by the U.S. DOE Office of Science Facilities at Brookhaven National Laboratory under Contract No. DE-SC0012704.

■ REFERENCES

(1) Min, H.; Lee, D. Y.; Kim, J.; Kim, G.; Lee, K. S.; Kim, J.; Paik, M. J.; Kim, Y. K.; Kim, K. S.; Kim, M. G.; et al. Perovskite solar cells with atomically coherent interlayers on SnO2 electrodes. *Nature* **2021**, *598*, 444−450.

(2) Xing, G.; Mathews, N.; Sun, S.; Lim, S. S.; Lam, Y. M.; Grätzel, M.; Mhaisalkar, S.; Sum, T. C. Long-range balanced electron-and hole-transport lengths in organic-inorganic CH3NH3PbI3. *Science* **2013**, *342*, 344−347.

(3) Shi, D.; Adinolfi, V.; Comin, R.; Yuan, M.; Alarousu, E.; Buin, A.; Chen, Y.; Hoogland, S.; Rothenberger, A.; Katsiev, K.; et al. Low trap-

state density and long carrier diffusion in organolead trihalide perovskite single crystals. *Science* **2015**, *347*, 519−522.

(4) Manser, J. S.; Christians, J. A.; Kamat, P. V. Intriguing optoelectronic properties of metal halide perovskites. *Chem. Rev.* **2016**, *116*, 12956−13008.

(5) Christians, J. A.; Miranda Herrera, P. A.; Kamat, P. V. Transformation of the excited state and photovoltaic efficiency of CH3NH3PbI3 perovskite upon controlled exposure to humidified air. *J. Am. Chem. Soc.* **2015**, *137*, 1530−1538.

(6) Juarez-Perez, E. J.; Hawash, Z.; Raga, S. R.; Ono, L. K.; Qi, Y. Thermal degradation of CH 3 NH 3 PbI 3 perovskite into NH 3 and CH 3 I gases observed by coupled thermogravimetry−mass spectrometry analysis. *Energy Environ. Sci.* **2016**, *9*, 3406−3410.

(7) Lee, J.-W.; Tan, S.; Seok, S. I.; Yang, Y.; Park, N.-G. Rethinking the A cation in halide perovskites. *Science* **2022**, *375*, No. eabj1186.

(8) Kim, J. Y.; Lee, J.-W.; Jung, H. S.; Shin, H.; Park, N.-G. High-efficiency perovskite solar cells. *Chem. Rev.* **2020**, *120*, 7867−7918.

(9) Zheng, X.; Wu, C.; Jha, S. K.; Li, Z.; Zhu, K.; Priya, S. Improved phase stability of formamidinium lead triiodide perovskite by strain relaxation. *ACS Energy Lett.* **2016**, *1*, 1014−1020.

(10) Jeon, N. J.; Noh, J. H.; Yang, W. S.; Kim, Y. C.; Ryu, S.; Seo, J.; Seok, S. I. Compositional engineering of perovskite materials for high-performance solar cells. *Nature* **2015**, *517*, 476−480.

(11) Saliba, M.; Matsui, T.; Domanski, K.; Seo, J.-Y.; Ummadisingu, A.; Zakeeruddin, S. M.; Correa-Baena, J.-P.; Tress, W. R.; Abate, A.; Hagfeldt, A.; Grätzel, M. Incorporation of rubidium cations into perovskite solar cells improves photovoltaic performance. *Science* **2016**, *354*, 206−209.

(12) Masi, S.; Gualdrón-Reyes, A. F.; Mora-Sero, I. Stabilization of black perovskite phase in FAPbI3 and CsPbI3. *ACS Energy Lett.* **2020**, *5*, 1974−1985.

(13) Zheng, E.; Niu, Z.; Tosado, G. A.; Dong, H.; Albrikan, Y.; Yu, Q. Revealing Stability of Inverted Planar MA-Free Perovskite Solar Cells and Electric Field-Induced Phase Instability. *J. Phys. Chem. C* **2020**, *124*, 18805−18815.

(14) Zhao, Q.; Hazarika, A.; Schelhas, L. T.; Liu, J.; Gaulding, E. A.; Li, G.; Zhang, M.; Toney, M. F.; Sercel, P. C.; Luther, J. M. Size-dependent lattice structure and confinement properties in CsPbI3 perovskite nanocrystals: negative surface energy for stabilization. *ACS Energy Lett.* **2020**, *5*, 238−247.

(15) Alaei, A.; Circelli, A.; Yuan, Y.; Yang, Y.; Lee, S. S. Polymorphism in metal halide perovskites. *Mater. Adv.* **2021**, *2*, 47−63.

(16) Swarnkar, A.; Marshall, A. R.; Sanehira, E. M.; Chernomordik, B. D.; Moore, D. T.; Christians, J. A.; Chakrabarti, T.; Luther, J. M. Quantum dot−induced phase stabilization of α-CsPbI3 perovskite for high-efficiency photovoltaics. *Science* **2016**, *354*, 92−95.

(17) Xue, J.; Lee, J.-W.; Dai, Z.; Wang, R.; Nuryyeva, S.; Liao, M. E.; Chang, S.-Y.; Meng, L.; Meng, D.; Sun, P.; et al. Surface ligand management for stable FAPbI3 perovskite quantum dot solar cells. *Joule* **2018**, *2*, 1866−1878.

(18) Wieliczka, B. M.; Márquez, J. A.; Bothwell, A. M.; Zhao, Q.; Moot, T.; VanSant, K. T.; Ferguson, A. J.; Unold, T.; Kuciauskas, D.; Luther, J. M. Probing the Origin of the Open Circuit Voltage in Perovskite Quantum Dot Photovoltaics. *ACS Nano* **2021**, *15*, 19334−19344.

(19) Bai, Y.; Hao, M.; Ding, S.; Chen, P.; Wang, L. Surface Chemistry Engineering of Perovskite Quantum Dots: Strategies, Applications, and Perspectives. *Adv. Mater.* **2022**, *34*, No. 2105958.

(20) Akkerman, Q. A.; Rainò, G.; Kovalenko, M. V.; Manna, L. Genesis, challenges and opportunities for colloidal lead halide perovskite nanocrystals. *Nat. Mater.* **2018**, *17*, 394−405.

(21) Wheeler, L. M.; Sanehira, E. M.; Marshall, A. R.; Schulz, P.; Suri, M.; Anderson, N. C.; Christians, J. A.; Nordlund, D.; Sokaras, D.; Kroll, T.; et al. Targeted ligand-exchange chemistry on cesium lead halide perovskite quantum dots for high-efficiency photovoltaics. *J. Am. Chem. Soc.* **2018**, *140*, 10504−10513.

(22) Hao, M.; Bai, Y.; Zeiske, S.; Ren, L.; Liu, J.; Yuan, Y.; Zarrabi, N.; Cheng, N.; Ghasemi, M.; Chen, P.; et al. Ligand-assisted cation-exchange engineering for high-efficiency colloidal Cs 1− x FA x PbI 3 quantum dot solar cells with reduced phase segregation. *Nat. Energy* **2020**, *5*, 79−88.

(23) Wang, Y.; Yuan, J.; Zhang, X.; Ling, X.; Larson, B. W.; Zhao, Q.; Yang, Y.; Shi, Y.; Luther, J. M.; Ma, W. Surface ligand management aided by a secondary amine enables increased synthesis yield of CsPbI3 perovskite quantum dots and high photovoltaic performance. *Adv. Mater.* **2020**, *32*, No. 2000449.

(24) Hu, L.; Zhao, Q.; Huang, S.; Zheng, J.; Guan, X.; Patterson, R.; Kim, J.; Shi, L.; Lin, C.-H.; Lei, Q.; et al. Flexible and efficient perovskite quantum dot solar cells via hybrid interfacial architecture. *Nat. Commun.* **2021**, *12*, No. 466.

(25) Xue, J.; Wang, R.; Chen, L.; Nuryyeva, S.; Han, T. H.; Huang, T.; Tan, S.; Zhu, J.; Wang, M.; Wang, Z. K.; et al. A small-molecule "charge driver" enables perovskite quantum dot solar cells with efficiency approaching 13%. *Adv. Mater.* **2019**, *31*, No. 1900111.

(26) Jodlowski, A. D.; Roldán-Carmona, C.; Grancini, G.; Salado, M.; Ralaiarisoa, M.; Ahmad, S.; Koch, N.; Camacho, L.; De Miguel, G.; Nazeeruddin, M. K. Large guanidinium cation mixed with methylammonium in lead iodide perovskites for 19% efficient solar cells. *Nat. Energy* **2017**, *2*, 972−979.

(27) Degani, M.; An, Q.; Albaladejo-Siguan, M.; Hofstetter, Y. J.; Cho, C.; Paulus, F.; Grancini, G.; Vaynzof, Y. 23.7% Efficient inverted perovskite solar cells by dual interfacial modification. *Sci. Adv.* **2021**, *7*, No. eabj7930.

(28) Hazarika, A.; Zhao, Q.; Gaulding, E. A.; Christians, J. A.; Dou, B.; Marshall, A. R.; Moot, T.; Berry, J. J.; Johnson, J. C.; Luther, J. M. Perovskite quantum dot photovoltaic materials beyond the reach of thin films: full-range tuning of A-site cation composition. *ACS Nano* **2018**, *12*, 10327−10337.

(29) Rühle, S. Tabulated values of the Shockley−Queisser limit for single junction solar cells. *Sol. Energy* **2016**, *130*, 139−147.

(30) Ball, J. M.; Petrozza, A. Defects in perovskite-halides and their effects in solar cells. *Nat. Energy* **2016**, *1*, No. 16149.

(31) Hoffman, J. M.; Strzalka, J.; Flanders, N. C.; Hadar, I.; Cuthriell, S. A.; Zhang, Q.; Schaller, R. D.; Dichtel, W. R.; Chen, L. X.; Kanatzidis, M. G. In situ grazing-incidence wide-angle scattering reveals mechanisms for phase distribution and disorientation in 2D halide perovskite films. *Adv. Mater.* **2020**, *32*, No. 2002812.

(32) Weller, M. T.; Weber, O. J.; Frost, J. M.; Walsh, A. Cubic perovskite structure of black formamidinium lead iodide, α-[HC (NH2) 2] PbI3, at 298 K. *J. Phys. Chem. Lett.* **2015**, *6*, 3209−3212.

(33) Protesescu, L.; Yakunin, S.; Kumar, S.; Bär, J.; Bertolotti, F.; Masciocchi, N.; Guagliardi, A.; Grotevent, M.; Shorubalko, I.; Bodnarchuk, M. I.; et al. Dismantling the "red wall" of colloidal perovskites: highly luminescent formamidinium and formamidinium−cesium lead iodide nanocrystals. *ACS Nano* **2017**, *11*, 3119−3134.

(34) Kagan, C. R.; Murray, C. B. Charge transport in strongly coupled quantum dot solids. *Nat. Nanotechnol.* **2015**, *10*, 1013−1026.

(35) Whitham, K.; Yang, J.; Savitzky, B. H.; Kourkoutis, L. F.; Wise, F.; Hanrath, T. Charge transport and localization in atomically coherent quantum dot solids. *Nat. Mater.* **2016**, *15*, 557−563.

(36) Li, Y.; Natakorn, S.; Chen, Y.; Safar, M.; Cunningham, M.; Tian, J.; Li, D. D.-U. Investigations on average fluorescence lifetimes for visualizing multi-exponential decays. *Front. Phys.* **2020**, *8*, No. 576862.

(37) Yang, Y.; Ostrowski, D. P.; France, R. M.; Zhu, K.; van de Lagemaat, J.; Luther, J. M.; Beard, M. C. Observation of a hot-phonon bottleneck in lead-iodide perovskites. *Nat. Photonics* **2016**, *10*, 53−59.

(38) Sum, T. C.; Mathews, N.; Xing, G.; Lim, S. S.; Chong, W. K.; Giovanni, D.; Dewi, H. A. Spectral Features and Charge Dynamics of Lead Halide Perovskites: Origins and Interpretations. *Acc. Chem. Res.* **2016**, *49*, 294−302.

(39) Fu, J.; Xu, Q.; Han, G.; Wu, B.; Huan, C. H. A.; Leek, M. L.; Sum, T. C. Hot carrier cooling mechanisms in halide perovskites. *Nat. Commun.* **2017**, *8*, No. 1300.

(40) Manser, J. S.; Kamat, P. V. Band filling with free charge carriers in organometal halide perovskites. *Nat. Photonics* **2014**, *8*, 737−743.

https://doi.org/10.1021/acsaem.2c01565

(41) Price, M. B.; Butkus, J.; Jellicoe, T. C.; Sadhanala, A.; Briane, A.; Halpert, J. E.; Broch, K.; Hodgkiss, J. M.; Friend, R. H.; Deschler, F. Hot-carrier cooling and photoinduced refractive index changes in organic-inorganic lead halide perovskites. *Nat. Commun.* **2015**, *6*, No. 8420.

(42) Kahmann, S.; Loi, M. A. Hot carrier solar cells and the potential of perovskites for breaking the Shockley−Queisser limit. *J. Mater. Chem. C* **2019**, *7*, 2471−2486.

(43) Hopper, T. R.; Gorodetsky, A.; Jeong, A.; Krieg, F.; Bodnarchuk, M. I.; Maimaris, M.; Chaplain, M.; Macdonald, T. J.; Huang, X.; Lovrincic, R.; Kovalenko, M. V.; Bakulin, A. A. Hot Carrier Dynamics in Perovskite Nanocrystal Solids: Role of the Cold Carriers, Nanoconfinement, and the Surface. *Nano Lett.* **2020**, *20*, 2271−2278.

(44) Zhang, J.; Zhang, L.; Zhang, Q. Unraveling the Effect of Surface Ligands on the Auger Process in an Inorganic Perovskite Quantum-Dot System. *J. Phys. Chem. Lett.* **2022**, *13*, 2943−2949.

(45) Li, M.; Bhaumik, S.; Goh, T. W.; Kumar, M. S.; Yantara, N.; Gratzel, M.; Mhaisalkar, S.; Mathews, N.; Sum, T. C. Slow cooling and highly efficient extraction of hot carriers in colloidal perovskite nanocrystals. *Nat. Commun.* **2017**, *8*, No. 14350.

(46) Papagiorgis, P.; Protesescu, L.; Kovalenko, M. V.; Othonos, A.; Itskos, G. Long-Lived Hot Carriers in Formamidinium Lead Iodide Nanocrystals. *J. Phys. Chem. C* **2017**, *121*, 12434−12440.

(47) Lim, J. W. M.; Giovanni, D.; Righetto, M.; Feng, M.; Mhaisalkar, S. G.; Mathews, N.; Sum, T. C. Hot Carriers in Halide Perovskites: How Hot Truly? *J. Phys. Chem. Lett.* **2020**, *11*, 2743−2750.

(48) Schnitzenbaumer, K. J.; Dukovic, G. Comparison of Phonon Damping Behavior in Quantum Dots Capped with Organic and Inorganic Ligands. *Nano Lett.* **2018**, *18*, 3667−3674.

(49) Richardson, G.; O'Kane, S. E.; Niemann, R. G.; Peltola, T. A.; Foster, J. M.; Cameron, P. J.; Walker, A. B. Can slow-moving ions explain hysteresis in the current−voltage curves of perovskite solar cells? *Energy Environ. Sci.* **2016**, *9*, 1476−1485.

(50) Guerrero, A.; Bisquert, J.; Garcia-Belmonte, G. Impedance spectroscopy of metal halide perovskite solar cells from the perspective of equivalent circuits. *Chem. Rev.* **2021**, *121*, 14430−14484.

(51) Azmi, R.; Ugur, E.; Seitkhan, A.; Aljamaan, F.; Subbiah, A. S.; Liu, J.; Harrison, G. T.; Nugraha, M. I.; Eswaran, M. K.; Babics, M.; et al. Damp heat−stable perovskite solar cells with tailored-dimensionality 2D/3D heterojunctions. *Science* **2022**, *376*, 73−77.

(52) Chen, J.; Jia, D.; Johansson, E. M.; Hagfeldt, A.; Zhang, X. Emerging perovskite quantum dot solar cells: feasible approaches to boost performance. *Energy Environ. Sci.* **2021**, *14*, 224−261.

(53) Jia, D.; Chen, J.; Qiu, J.; Ma, H.; Yu, M.; Liu, J.; Zhang, X. Tailoring solvent-mediated ligand exchange for CsPbI3 perovskite quantum dot solar cells with efficiency exceeding 16.5%. *Joule* **2022**, *6*, 1632−1653.

(54) Li, F.; Zhou, S.; Yuan, J.; Qin, C.; Yang, Y.; Shi, J.; Ling, X.; Li, Y.; Ma, W. Perovskite quantum dot solar cells with 15.6% efficiency and improved stability enabled by an α-CsPbI3/FAPbI3 bilayer structure. *ACS Energy Lett.* **2019**, *4*, 2571−2578.